ADVANCED MATERIALS
www.advmat.de

Artificial Phages with Biocatalytic Spikes for Synergistically Eradicating Antibiotic-Resistant Biofilms

Sutong Xiao, Lan Xie, Yang Gao, Mao Wang, Wei Geng, Xizheng Wu, Raul D. Rodriguez, Liang Cheng, Li Qiu, and Chong Cheng**

Antibiotic-resistant pathogens have become a global public health crisis, especially biofilm-induced refractory infections. Efficient, safe, and biofilm microenvironment (BME)-adaptive therapeutic strategies are urgently demanded to combat antibiotic-resistant biofilms. Here, inspired by the fascinating biological structures and functions of phages, the de novo design of a spiky Ir@Co_3O_4 particle is proposed to serve as an artificial phage for synergistically eradicating antibiotic-resistant *Staphylococcus aureus* biofilms. Benefiting from the abundant nanospikes and highly active Ir sites, the synthesized artificial phage can simultaneously achieve efficient biofilm accumulation, extracellular polymeric substance (EPS) penetration, and superior BME-adaptive reactive oxygen species (ROS) generation, thus facilitating the in situ ROS delivery and enhancing the biofilm eradication. Moreover, metabolomics found that the artificial phage obstructs the bacterial attachment to EPS, disrupts the maintenance of the BME, and fosters the dispersion and eradication of biofilms by down-regulating the associated genes for the biosynthesis and preservation of both intra- and extracellular environments. The in vivo results demonstrate that the artificial phage can treat the biofilm-induced recalcitrant infected wounds equivalent to vancomycin. It is suggested that the design of this spiky artificial phage with synergistic "penetrate and eradicate" capability to treat antibiotic-resistant biofilms offers a new pathway for bionic and nonantibiotic disinfection.

1. Introduction

The emergence and proliferation of antibiotic-resistant pathogens has been established as a global public health crisis, dramatically escalating morbidity and mortality.[1–4] Notably, ≈80% of stubborn and refractory infections are intimately associated with biofilm formation.[5–7] In contrast to planktonic bacteria, the biofilms are equipped with a dense shield of extracellular polymeric substance (EPS) [8] and a biofilm microenvironment (BME) replete with acidity and H_2O_2,[9,10] which can effectively safeguard the bacteria against host immune defenses and impede the penetration of antibacterial agents.[11,12] Furthermore, the biofilm can alter the phenotype of encapsulated bacteria and stimulate the formation of persistent bacteria,[13,14] thus rendering great challenges to the current antibacterial therapies. Consequently, innovative strategies are urgently demanded to actualize BME-adaptive full-stage eradication of drug-resistant bacterial biofilm, such as the photothermal responsive

S. Xiao, L. Xie, Y. Gao, M. Wang, W. Geng, L. Qiu, C. Cheng
College of Polymer Science and Engineering
State Key Laboratory of Polymer Materials Engineering
Department of Medical Ultrasound
West China Hospital
Sichuan University
Chengdu 610065, China
E-mail: qiulihx@scu.edu.cn; chong.cheng@scu.edu.cn, chong.cheng@fu-berlin.de

X. Wu
Max Planck Institute for Chemical Physics of Solids
01187 Dresden, Germany

R. D. Rodriguez
Tomsk Polytechnic University
Lenin ave. 30, Tomsk 634050, Russia

L. Cheng
Department of Materials Science and Engineering
The Macau University of Science and Technology
Taipa, Macau 999078, China

C. Cheng
Department of Endodontics
Department of Orthodontics
State Key Laboratory of Oral Diseases & National Clinical Research Center for Oral Diseases
West China Hospital of Stomatology
Sichuan University
Chengdu 610041, China

The ORCID identification number(s) for the author(s) of this article can be found under https://doi.org/10.1002/adma.202404411

DOI: 10.1002/adma.202404411

nanoparticles[15] and immuno-activation antibacterial nanosystems.[16,17] Although high biofilm eradication properties have been achieved, these methods are still too complex, and additional treatments are usually needed. The construction of facile and BME-adaptive therapeutic strategies may offer a new paradigm to treat antibiotic-resistant biofilm-related recalcitrant infected wounds.

Recent advancements in reactive oxygen species (ROS)-related biocatalytic therapies provide a new promising avenue for combating drug-resistant bacterial biofilm and refractory wound infections.[18] By generating highly toxic ROS, the biocatalytic materials can potentially overcome bacterial resistance and have comparable therapeutic effects as conventional antibiotics.[19,20] Among diverse biocatalytic materials, such as nanocarbon-based or polymer-based enzyme-mimics,[21] metal oxide-based biocatalysts have received extensive attention due to their excellent biocompatibility, structural diversity, feasible modification, tunable catalytic sites, and low cost when compared to the other materials-based biocatalysts. For instance, the Fe-doped MoO_x nanoflowers can significantly enhance ROS production,[22] oxygen-deficient S-doped TiO_2 can be used for photocatalytic disinfection,[23] MoO_2/WO_3 heterojunction particles show high efficiency in treating bacteria-induced osteomyelitis via microwave irradiation,[24] and Cu-porphyrin modified-Fe_2O_3 2D nanosheet exhibits broad-spectrum inhibition activity against oral pathogens via ROS and released ions.[25]

Although significant achievements have been made in treating planktonic bacteria,[26,27] the application of metal oxide-based ROS biocatalysts for combating biofilm still encounters several challenges,[28] including a relatively low ROS production activity, extremely short half-lives of toxic ROS, and most importantly limited adhesion and penetration capabilities, which severely restrict their oxidative damage and biofilm eradication activity.[29,30] Even though it remains a substantial challenge, it is highly desirable to design metal oxide-based biocatalysts with integrated high ROS generation activity, excellent biofilm accumulation, and efficient penetration capacities to facilitate the BME-adaptive treatments of antibiotic-resistant biofilms.[31,32] In nature, abundant microorganisms have evolved distinctive biological structures and morphologies conducive to predation and defense.[33–35] For instance, phage viruses with multiple tail-spike structures function as specialized predators of bacterial hosts, which efficiently recognize and capture bacteria and ultimately trigger bacterial lysis. Ideally, creating metal oxide-based ROS biocatalysts with phage-like spiky structures and biofunctions would engage directly with the biofilm to fundamentally destabilize and loosen their dense shield compositions.

Inspired by the fascinating biological structures and functions of phages,[36–38] here, we propose the de novo design of a spiky Ir@Co_3O_4 (S) particle to serve as an artificial phage for synergistically eradicating antibiotic-resistant biofilms (**Figure 1**). The primary motivation for this study derives from two concepts: 1) design metal oxide-based biocatalysts with abundant nanospikes that are capable of accumulating and penetrating the bacterial biofilm, thus triggering the severe biofilm disruption; 2) create highly active Ir catalytic sites with potent electronic coupling by Co—O—Ir structure in Ir@Co_3O_4 (S) that can enable the synthesized nanospikes to rapidly respond to the BME to generate ROS, and function as an artificial phage with the synergistic "penetrate and eradicate" effects to combat biofilms. The superior and potent peroxidase (POD)- and oxidase (OXD)-mimetic ROS production capacities and mechanisms of these spiky Ir@Co_3O_4 (S) particles have been carefully investigated by combining diverse experimental and theoretical approaches. Systematic in vitro studies demonstrate that the spiky structure plays an essential part in bacterial capture, biofilm accumulation, and penetration, which eventually induces hole structure to facilitate the in situ ROS delivery and enhance biofilm eradication. Moreover, metabolomics found that the accumulation of Ir@Co_3O_4 (S) particles obstructs the bacterial attachment to EPS, disrupts the maintenance of the cellular environment, and promotes the dispersion and eradication of biofilms by down-regulating the associated genes for the biosynthesis and preservation of both intra- and extracellular environments. Our in vivo results corroborate that the synthesized artificial phage can eradicate biofilm and expedite wound healing with therapeutic effectiveness equivalent to vancomycin. The proposed synergistic "penetrate and eradicate" therapeutic strategy by artificial phages offers a promising paradigm to advance the treatment of recalcitrant infected wounds and other antibiotic-resistant biofilm infection-related therapies.

2. Results and Discussion

In a typical synthesis procedure, an iridium/cobalt carbonate hydroxide precursor with spiky morphology was synthesized via a one-pot hydrothermal coprecipitation method, accompanied by subsequent pyrolysis-activation process to obtain spiky Ir@Co_3O_4 (S) particles (named Ir@Co_3O_4 (S)) to serve as artificial phages. For comparison, a claviform-shaped Ir@Co_3O_4 (named Ir@Co_3O_4 (C)) was fabricated by employing a probe sonicator to destroy the spiky structure of Ir@Co_3O_4 (S) (Figure S1, Supporting Information). Scanning electron microscopy (SEM) and transmission electron microscopy (TEM) spectra reveal that Ir@Co_3O_4 (S) adopts a spiky morphology consisting of uniformly sharp nanoscale bristles radiating from the center outward (**Figure 2**a,b; and Figures S2–S4, Supporting Information). The control samples, pristine Co_3O_4 and Ir@Co_3O_4 (C), both exhibit a fragmented claviform structure. Meanwhile, the average size of Ir@Co_3O_4 (S) is measured to be around 5 µm in dynamic light scattering (DLS) (Figure S5, Supporting Information). Thereafter, the selected area electron diffraction (SAED) pattern preliminarily clarified the crystalline structure of the nanospikes (Figure S6, Supporting Information).[39] The high-resolution TEM (HR-TEM) images in Ir@Co_3O_4 (S) further deliver detailed lattice patterns with interplanar spacings of 0.244 and 0.286 nm, well-matched to the (311) and (220) facets of Co_3O_4 nanocrystals, respectively, in accordance with the fast Fourier transform (FFT) image (Figure 2c). The X-ray powder diffraction (XRD, Figure 2d) pattern demonstrates that the as-prepared Ir@Co_3O_4 (S) maintains a face-centered cubic symmetry pattern of Co_3O_4 (space group: *Fd-3m*) [40,41] with no detection of Ir phase (Figure 2e; and Table S1, Supporting Information).

High-angle annular dark field-scanning TEM (HAADF-STEM) has been carried out for Ir@Co_3O_4 (S), as illustrated in Figure 2f, which exhibits a high density of ultrasmall Ir nanoclusters uniformly dispersed on the surface of Co_3O_4 crystals. Atomic-resolution HAADF-STEM images visually provide the precise periodic arrangements of Ir sites (Figure 2g). Subsequently, the

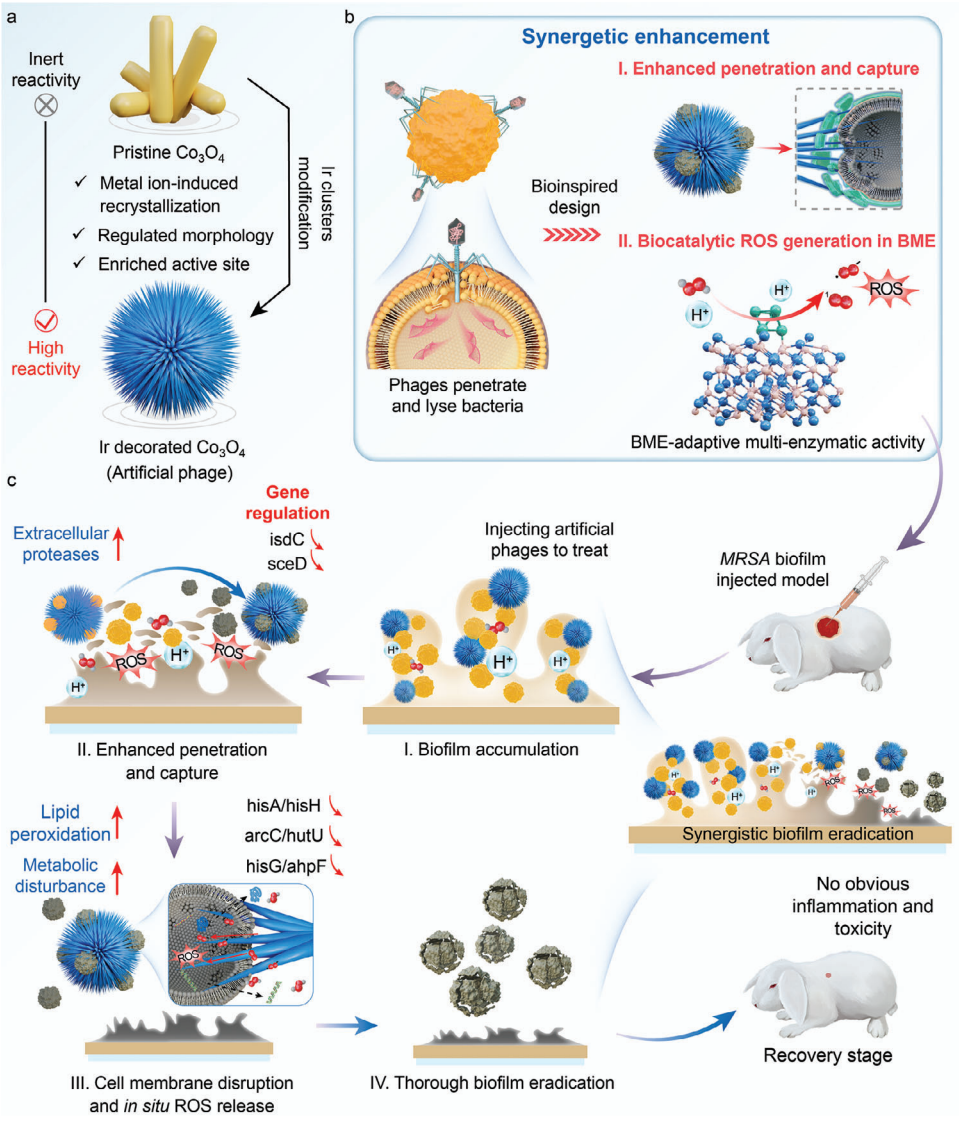

Figure 1. Design of artificial phages with biocatalytic spikes for synergistic biofilm eradication. a) Fabrication process of spiky Ir@Co_3O_4 (S) particles to serve as artificial phages. b) Schematic diagram of the bioinspired and BME-adaptive artificial phages, and c) the treatment processes and mechanisms of artificial phages for disintegrating the biofilm of antibiotic-resistant pathogens and promoting wound healing.

energy-dispersive X-ray (EDX) elemental mapping analysis highlights the homogeneous spatial distribution of Ir, Co, and O elements throughout Ir@Co_3O_4 (S) (Figure 2h; and Figure S7, Supporting Information). Comprehensive surface structural information of Ir@Co_3O_4 (S) was also obtained from Raman spectroscopy (Figure 2i). The fabricated samples present the characteristic peaks of Co_3O_4,[42] while the E_g vibrational mode at ≈678 cm^{-1} exhibits a substantial blueshift relative to pristine Co_3O_4, suggesting lattice strain and a more disordered phase on the surface due to the modification of Ir clusters.

Afterward, X-ray photoelectron spectroscopy (XPS) was conducted to probe the local coordination environments and electronic structures of Ir@Co_3O_4 (S). The survey XPS spectra demonstrate the presence of Ir, Co, and O with similar Ir: Co molar ratios (0.0176 in Ir@Co_3O_4 (S) and 0.0180 in Ir@Co_3O_4 (C)) (Figure S8, Supporting Information). The high-resolution Ir 4*f* spectrum can be deconvoluted into two doublets centered at 61.21/64.31 and 61.89/65.29 eV, labeled as Ir^0 and Ir^{n+}, respectively, which indicates that Ir precursor is partially reduced to metallic Ir (Figure 2j). The peak at 60.6 eV is attributed to the orbital overlap of Co 3*p*. Notably, the Ir species in Ir@Co_3O_4 (C) maintain remarkably comparable electronic structures (Figure S9, Supporting Information). As revealed in Figure 2k; and Figure S10, and Table S2, Supporting Information, the primary peak signals of Co 2*p* are recognized as Co^{2+} and Co^{3+}, respectively.[43–45] Concurrently, the Co^{2+}/Co^{3+} intensity ratio in Ir@Co_3O_4 (S) is 0.466, which is much smaller than pristine Co_3O_4 (0.940). Taken together, we deduce that there are distinct, robust interactions and substantial electron transfer between Ir clusters and Co_3O_4, thereby enabling the stable anchor of Ir clusters.[46] Further assessment of the O 1*s* spectra of Ir@Co_3O_4 (S) and Ir@Co_3O_4 (C) unveils a larger lattice oxygen M—O

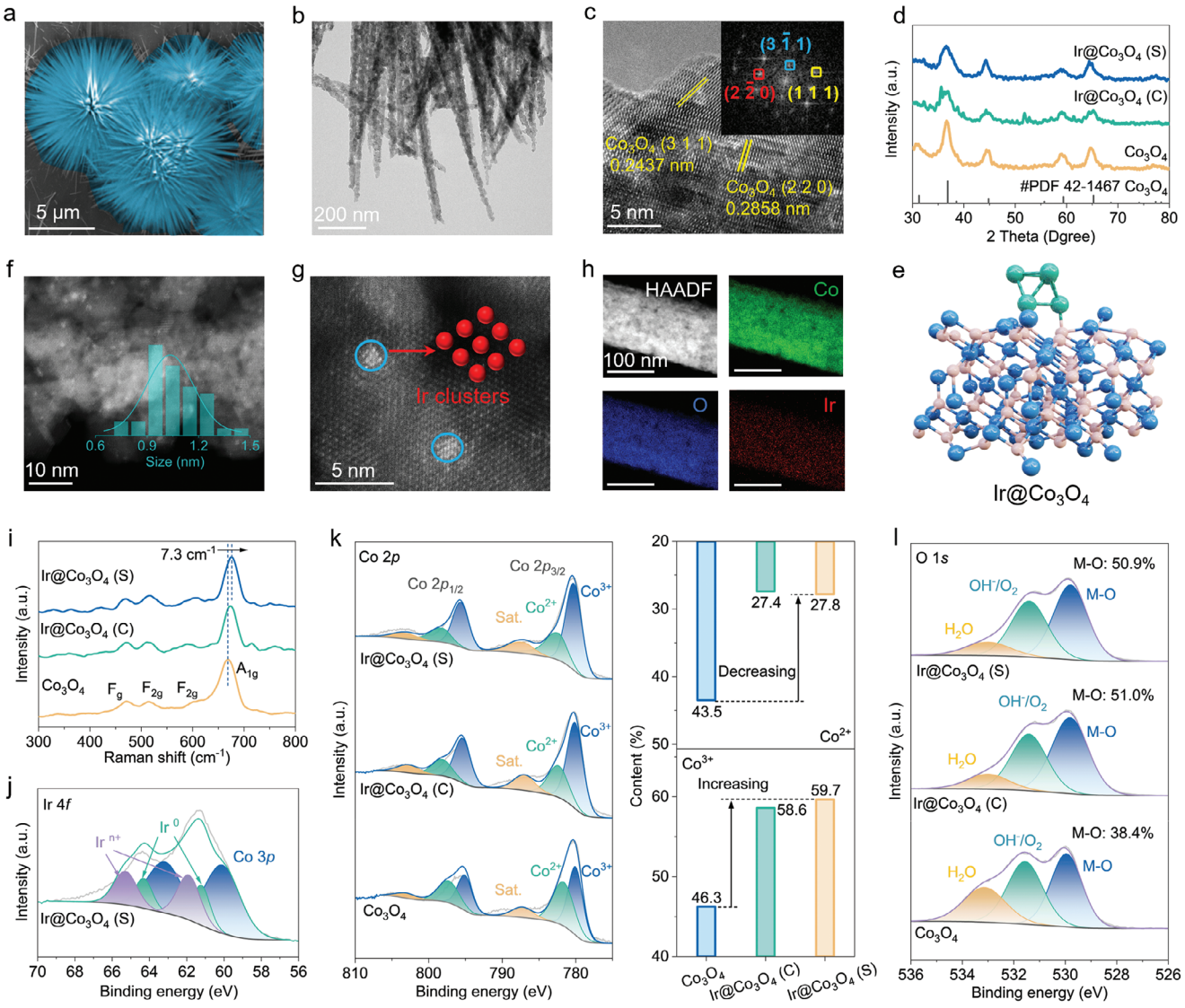

Figure 2. Material synthesis and characterization. a) SEM image of Ir@Co_3O_4 (S). b) TEM image of the spiky structure of Ir@Co_3O_4 (S). c) HR-TEM image of Ir@Co_3O_4 (S). The inset shows the FFT image. d) XRD patterns of Co_3O_4, Ir@Co_3O_4 (C), and Ir@Co_3O_4 (S). e) Crystal-structural diagram of Ir@Co_3O_4. f,g) Atomic-scale HAADF-STEM images of Ir@Co_3O_4 (S). h) The EDS elemental mapping images of Ir@Co_3O_4 (S). Experiments were repeated independently (a–c, f–h) three times with similar results. i) The Raman spectra of Co_3O_4, Ir@Co_3O_4 (C), and Ir@Co_3O_4 (S). The XPS survey scan spectra of Co_3O_4, Ir@Co_3O_4 (C), and Ir@Co_3O_4 (S) in j) Ir 4*f*, k) Co 2*p*, and l) O 1*s* regions. a.u. indicates the arbitrary units.

concentration in comparison to Co_3O_4 (Figure 2l; and Table S3, Supporting Information), which can be ascribed to the doping by the Ir species, demonstrating the occurrence of potent electronic coupling at the interface by Co—O—Ir bonding.[41]

Upon elucidating the morphologies and chemical structures of Co_3O_4, Ir@Co_3O_4 (C), and Ir@Co_3O_4 (S), we performed a comprehensive assessment of their POD- and OXD-mimetic biocatalytic performances utilizing the universal 3,3,5,5-tetramethylbenzidine (TMB) colorimetric assay.[47,48] The Ir@Co_3O_4 (S) and Ir@Co_3O_4 (C) exhibit similarly superior POD- and OXD-mimetic activities, while Co_3O_4 exhibits nearly no ROS production activity (**Figure** 3a; and Figure S11, Supporting Information). Moreover, the pH-dependent POD- and OXD-mimetic ROS production activities of Ir@Co_3O_4 (S) have also been detected to demonstrate its high BME-adaptivity, suggesting that the synthesized artificial phages mainly produce ROS in biofilm-infected regions, while they show no ROS generation in normal tissue environments (Figure 3b; and Figures S12 and S13, Supporting Information). Besides, the stability of Ir@Co_3O_4 (S) was evaluated, revealing a consistent maintenance of its characteristic spiky morphology and continuous ROS-generating capability, which further highlights the superior potential of Ir@Co_3O_4 (S) in sustaining prolonged therapeutic efficiency for full-stage biofilm eradication (Figure S14, Supporting Information). Subsequently, the catalytic constant (K_m), maximal reaction velocity (V_{max}), and turnover number (TON) are systematically explored (Figures S15 and S16, Supporting Information).[49,50] Compared to the low activity of Co_3O_4 ($V_{max} = 1.38$ and TON = 3.40×10^{-3}),

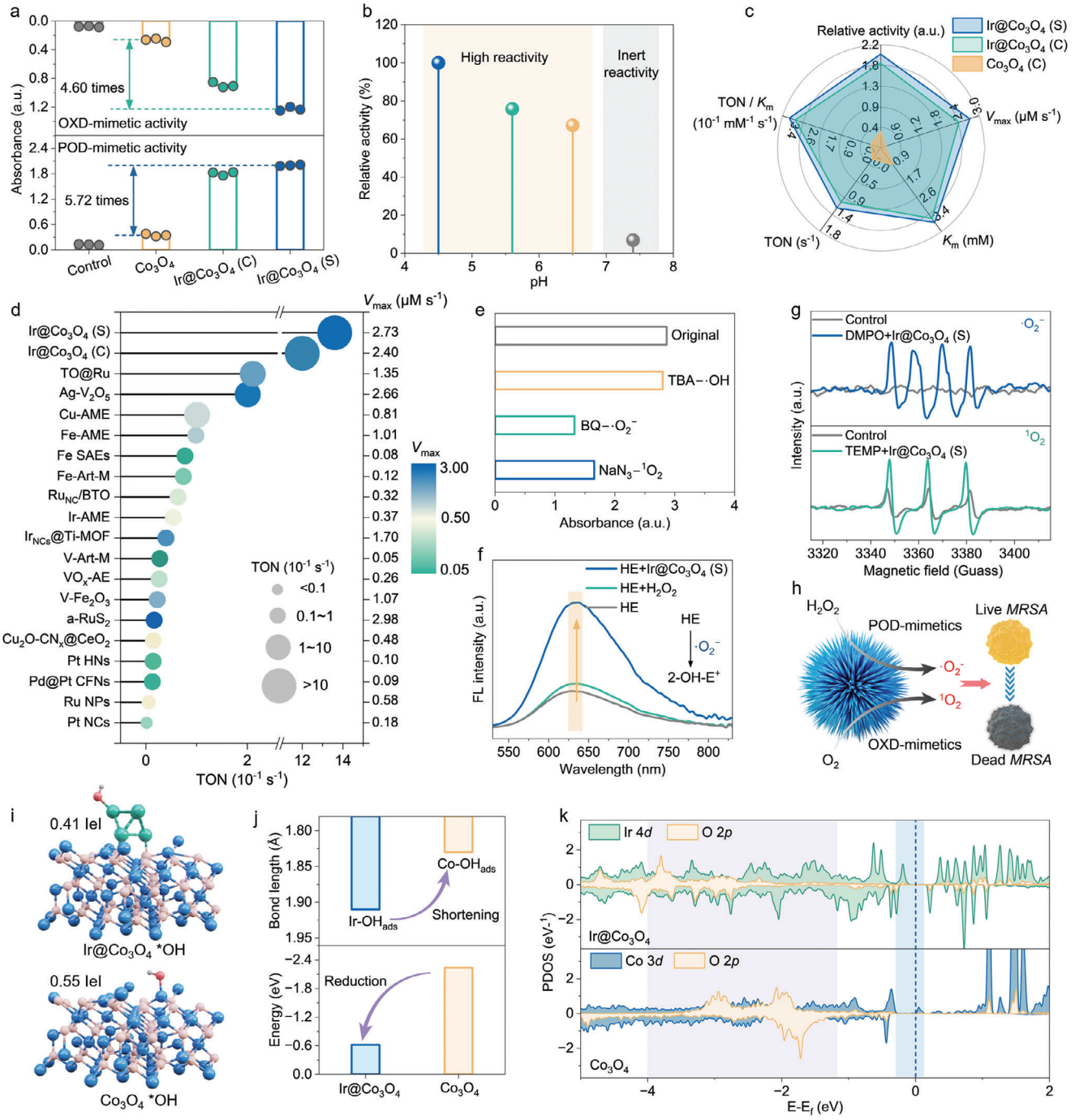

Figure 3. Detection of the ROS-related biocatalytic performances. a) POD- and OXD-mimetic activities employing TMB-based UV–vis spectra in the presence of biocatalytic materials. Data are expressed as mean ± SD (n = 3 independent experiments, data are presented as mean ± S.D.). b) pH effects of the POD-mimetic activity of $Ir@Co_3O_4$ (S). c) Kinetic parameters in biocatalytic materials. d) Comparison and analysis of the TON and V_{max} values with previously published state-of-the-art enzyme-mimetic materials. e) The free radical quenching experiments, tert-butyl alcohol (TBA), p-benzoquinone (BQ), and sodium azide (NaN_3) were utilized as quenching agents for •OH, $•O_2^-$, and $^1O_2$, respectively. f) The $•O_2^-$ generation ability in the presence of H_2O_2 tested by HE assay. g) EPR spectra for recording the $•O_2^-$ and $^1O_2$ signals. h) Schematic process of the $Ir@Co_3O_4$ (S) induced enzyme-mimicking ROS production for bacterial disinfection. i) Crystal-structural diagram of $Ir@Co_3O_4$*OH and Co_3O_4*OH. j) Bond lengths and adsorption energies of $Ir@Co_3O_4$ and Co_3O_4 in interaction with *OH. k) Calculated PDOS of Co 3d and Ir 4d orbitals with O 2p orbital in *OH. a.u. indicates the arbitrary units.

the Ir@Co_3O_4 (S) (V_{max} = 27.27 and TON = 1.36), and Ir@Co_3O_4 (C) (V_{max} = 23.98 and TON = 1.20) present superior POD-like catalytic kinetics (Figure 3c; and Figure S17, Supporting Information). Ir@Co_3O_4 (S) also displays superior enzymology indexes across the other reported state-of-the-art POD-mimics that include metal oxides, metal nanoparticles, single-atom enzyme analogs, and metal–organic frameworks (Figure 3d; and Table S4, Supporting Information). Furthermore, we have extended the same preparation approach to a series of other noble metals with a similar large *d*-electron wave-function spatial range as Ir supported onto Co_3O_4. Notably, Ir@Co_3O_4 (S) demonstrates a markedly superior capacity to generate ROS (Figure S18, Supporting Information).

Furthermore, the free radical quenching experiment was initially conducted to elucidate the generated species of ROS, which could be identified as $^1O_2$ and $\bullet O_2^-$ (Figure 3e; and Figure S19, Supporting Information).[51,52] Subsequently, the presence of $\bullet O_2^-$ has been confirmed by a hydroethidine (HE) probe (Figure 3f; and Figure S20, Supporting Information),[53] and the $^1O_2$ species can be detected by the 9,10-diphenanthraquinone (DPA) in a time-dependent manner (Figure S21, Supporting Information). In addition, adopting 5,5-dimethyl-1-pyrroline *N*-oxide (DMPO) and 2,2,6,6-tetramethylpiperidine (TEMP) as the specific spin trap reagents, the electron paramagnetic resonance (EPR) measurements verify the significant production of $\bullet O_2^-$ and $^1O_2$ under mildly acidic conditions (Figure 3g).[54,55] Collectively, modifying Ir sites will enable the synthesized spiky artificial phages to rapidly respond to the BME to generate ROS; thus, it may effectively combat biofilm-associated infections induced by antibiotic-resistant pathogens (Figure 3h).

We carried out density functional theory (DFT) calculations to elucidate the underlying mechanism of the rapid reaction kinetics occurring at the biocatalytic Ir sites. Primary investigations utilizing constructive modeling indicate substantial electron transfer between Ir sites and Co_3O_4 substrates, which is mediated via interfacial Co—O—Ir bonds (Figure S22, Supporting Information). Based on our previous studies, H_2O_2 undergoes decomposition during the POD-like reaction to generate two *OH intermediates that attach to reaction sites.[56] Therefore, we thoroughly analyzed the crucial intermediate of Ir*OH and Co*OH. As evidenced by the comparison of charge density difference analysis and Bader charge, the charge transfer of Ir@Co_3O_4 (0.41 |e|) interacting with *OH is noticeably smaller than that of Co_3O_4 (0.55 |e|) (Figure 3i; and Figure S23, Supporting Information), which implies a more reactive state with a weaker affinity and binding force toward oxygen intermediates. Besides, analyses of bond length and adsorption energy indicate that the processes of oxygen intermediate adsorption and desorption preferentially occur at the Ir sites (Figure 3j). Moreover, the Ir 4*d* / Co 3*d*-O 2*p* orbitals interactions within *OH were assessed employing the partial density of states (PDOS), revealing that the Ir 4*d* orbitals maintain a higher density of states with the O 2*p* orbitals near the Fermi energy level (Figure 3k), which yields an enhanced reactivity and is notably consistent with our experimental results. To sum up, the unique spiky morphology and the efficient and BME-adaptive ROS generation capability of Ir@Co_3O_4 (S) can function as an artificial phage with synergistic "penetrate and eradicate" effects to combat bacteria and biofilms, which will be thoroughly elaborated in the following studies.

Encouraged by the unique spiky morphology and superior ROS-generating properties of Ir@Co_3O_4 (S), we subsequently explored its bionic ability as an artificial phage to capture and kill drug-resistant planktonic bacteria. All antibacterial experiments were based on methicillin-resistant *Staphylococcus aureus* (*MRSA*). As shown in **Figure 4**a,b, the different morphologies of Ir@Co_3O_4 (S) and Ir@Co_3O_4 (C) offer these materials with distinct interactions with bacteria. SEM and TEM images visualize that the spiky nanostructures of Ir@Co_3O_4 (S) can effectively penetrate the bacterial cell walls and lipid membranes, establishing a secure and localized capture of *MRSA*.[57] The visible distortion and morphological collapse indicate the irreversible destruction (Figure 4c). In contrast, the fragmented claviform Co_3O_4 and Ir@Co_3O_4 (C) exhibit poor bacterial capture capacity, preferring to adhere to the bacterial surface and thus causing slight damage to bacteria (Figure 4d; and Figures S24 and S25, Supporting Information). Moreover, we calculated the bacterial content after incubation with materials under different incubation conditions. The Ir@Co_3O_4 (S) treated group (Figure 4e) can significantly decrease the bacteria concentration, which is considerably faster than the Ir@Co_3O_4 (C) treated group (Figure 4g). Besides, the minimal inhibit concentration (MIC) and minimum bactericidal concentration (MBC) obtained for the Ir@Co_3O_4 (S) treated group are both 0.08 mg mL^{-1}, which are significantly lower than that of Ir@Co_3O_4 (C) (MIC: 0.2 mg mL^{-1} and MBC: 0.32 mg mL^{-1}) and Co_3O_4 (MIC: more than 0.5 mg mL^{-1} and MBC: more than 0.32 mg mL^{-1}) (Figures S26 and S27, Supporting Information).[58,59] Subsequent spread plate results further clearly demonstrate that Ir@Co_3O_4 (S) has a capture and killing potency of ≈100%, remarkably superior to the 36.3% of Ir@Co_3O_4 (C) (Figure 4f,h; and Figures S28 and S29, Supporting Information). Overall, the spiky structures play an essential part in bacterial capture and promote a synergistic and effective sterilization capability in conjunction with in situ ROS generation.

Thereafter, 3D reconstructions of Live/Dead detections were also performed utilizing fluorescence microscopy and a confocal laser scanning microscope (CLSM).[60] As shown in Figure 4i; and Figure S30, Supporting Information, the Ir@Co_3O_4 (S) treated group expresses notably intense red fluorescence in the appearance of aggregates, confirming that a substantial amount of *MRSA* has been efficiently captured and lethally killed. Conversely, the Ir@Co_3O_4 (C) treated group maintains a sufficiently high survival rate. The protein leakage assay also offers convincing evidence of *MRSA* membrane structure disruption and cytoplasmic leakage, with the highest degree of lipid membrane permeability in the Ir@Co_3O_4 (S) treated group (Figure 4k). Subsequently, to further verify whether a large amount of ROS released by Ir@Co_3O_4 (S) in response to BME could oxidize the lipids of *MRSA* cell membranes, a lipid peroxidation probe, C11-BODIPY$^{581/591}$, was labeled to detect the accumulation of lipid peroxides (LPO) (Figure 4l; and Figure S31, Supporting Information).[61] CLSM images indicate that the Ir@Co_3O_4 (S) treated group demonstrates the strongest green fluorescence, implying that it induces the most severe lipid peroxidation. These results lead us infer that the fabricated spiky artificial phage synergistically accomplishes thorough killing of *MRSA* bacteria involving two pathways: 1) the spikes are capable of capturing and puncturing the bacteria, triggering the severe cell membrane

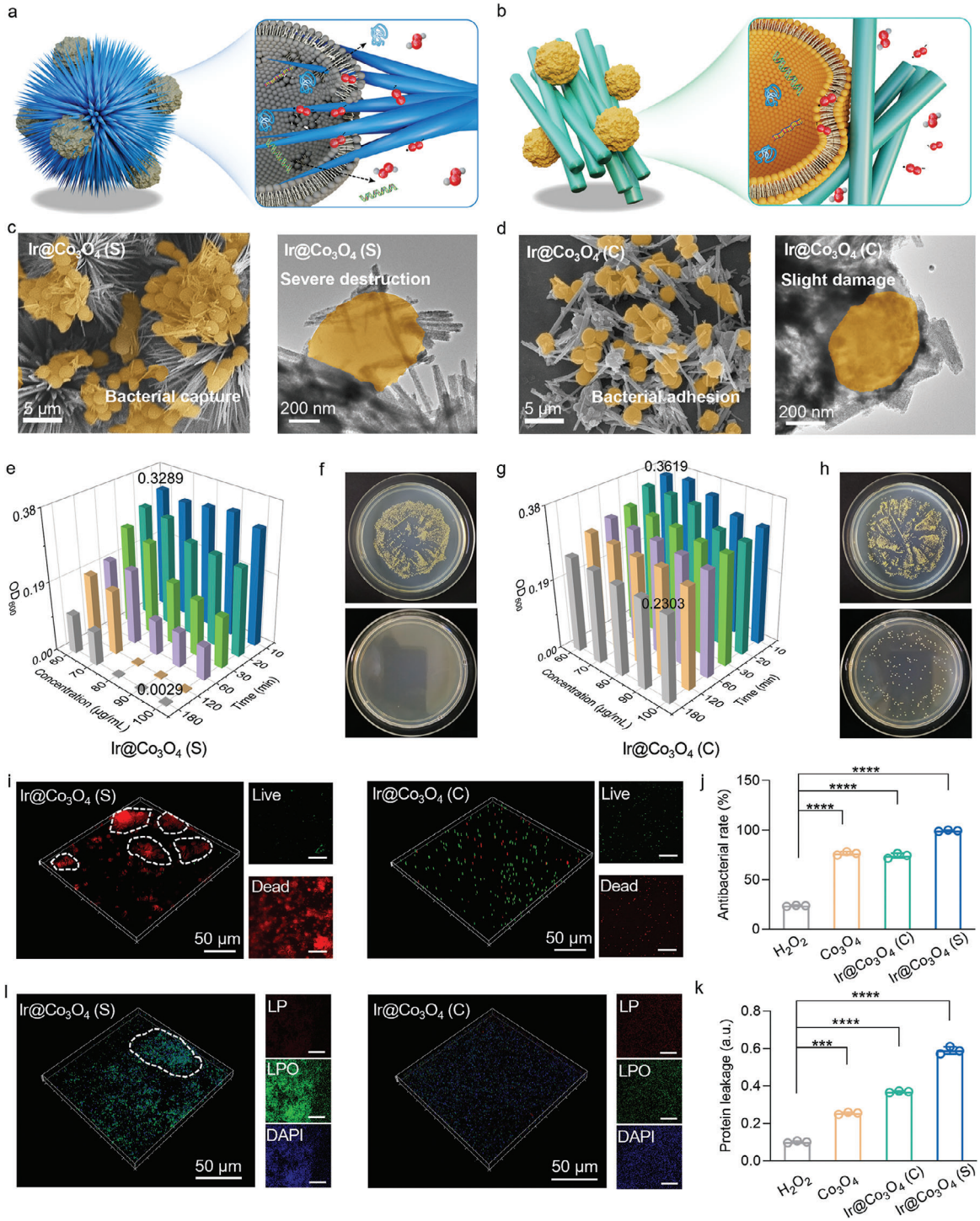

Figure 4. Evaluation of in vitro bactericidal actions on planktonic *MRSA*. Schematic illustration of the bactericidal mechanism of a) spiky Ir@Co_3O_4 (S) and b) claviform Ir@Co_3O_4 (C). Representative SEM and TEM images of the bacteria after cultivation with Ir@Co_3O_4 (S) c) and Ir@Co_3O_4 (C) d). The bacterial viabilities of captured *MRSA* toward the incubation time and concentration of Ir@Co_3O_4 (S) e), Ir@Co_3O_4 (C) g). OD_{600} values are positively correlated with the number of bacteria in the solution. The spread plate of *MRSA* before (above) and after (below) dispersing Ir@Co_3O_4 (S) f) and Ir@Co_3O_4 (C) h). i) 3D CLSM images of bacteria incubated with Ir@Co_3O_4 (S) and Ir@Co_3O_4 (C), Green: live bacteria, Red: dead bacteria (scale bar: 50 μm). j) Statistics on the antibacterial effects of agar plates ($n = 3$ biologically independent replicates). k) Detection of bacterial protein leakage ($n = 3$ biologically independent replicates). l) C11-BODIPY$^{581/591}$ fluorescence labeled images of bacteria (scale bar: 50 μm). Experiments were repeated independently c-i,l) three times with similar results. Data are expressed as mean ± S.D. The assessment of *P*-values is performed through the utilization of one-way analysis of variance (ANOVA). Indication of significant differences is marked by asterisks (*$P < 0.05$, **$P < 0.01$, ***$P < 0.001$, ****$P < 0.0001$, ns represented nonsignificance). a.u. indicates the arbitrary units.

disruption and leakage of intracellular substances; 2) the Ir sites catalyze the accumulation of ROS, along with the potent penetration of the spiky structure, Ir@Co_3O_4 (S) can achieve the in situ release of ROS and facilitate bacterial death.

Biofilms generated by pathogenic bacteria are a primary factor in many chronic infectious diseases.[7,62] Benefiting from the low pH and enriched H_2O_2 of BME, the inherent physiological heterogeneity within biofilms substantially weakens the antibacterial effectiveness of antibiotics, thereby promoting antibiotic resistance.[7,63] Among them, an efficient nanoparticle permeation implemented within the dense protective layer of biofilms is a crucial prerequisite for the dispersion and ROS oxidative eradication of biofilms.[16] To theoretically evaluate the accumulation and penetration of Ir@Co_3O_4 (S) into mature biofilms, we constructed an all-atom molecular dynamics model to explore the puncture behavior of spiky and plate-like structures on EPS and lipid bilayer (**Figure** 5a).[64] As the transmembrane mode simulations displayed in Figure 5b, a constant force is applied to the spike/plate-like materials to approach the membrane to simulate the puncture phenomenon. As the simulation time progresses, the spiky material migrates along the pores and eventually achieves the penetration of the EPS and lipid bilayer. The *z*-axis top view indicates that the position of the spiky material shifts significantly during the penetration of the EPS and lipid bilayer, forming a visible pore structure, in contrast to the constant surface position of the plate-like material. By quantifying of the EPS density (Figure S32, Supporting Information) and the interaction force (Figure 5c), we found that the spiky structure undergoes a pronounced change in EPS density during the penetration process and exhibits significant interaction with both EPS and the lipid bilayer. Conversely, the plate-like material experiences only a limited change that can be considered negligible compared to the spike case.

Following that, we comprehensively evaluated the biofilm eradication effects of Ir@Co_3O_4 (S) by diverse experimental methods. As visualized by Live/Dead staining, the Ir@Co_3O_4 (S) displays a substantial reduction in the number of live bacteria and the integrity of the biofilm is extensively compromised with an evident decrease in thickness. In contrast, Ir@Co_3O_4 (C)-treated biofilms remain relatively intact with a thicker state (Figure 5d; and Figure S33, Supporting Information). Crystal violet staining also reveals a 90% reduction in biofilm biomass, supporting its superior biofilm removal ability (Figure 5e,f). Subsequently, the Alexa Fluor 647-dextran labeled biofilm matrix indicates that the Ir@Co_3O_4 (S) can apparently reduce the EPS levels (labeled in blue) with an elimination rate close to 100%, which is more efficient than the Ir@Co_3O_4 (C) (Figure 5g,h; and Figures S34 and S35, Supporting Information). Additionally, the C11-BODIPY$^{581/591}$ CLSM images show that the Ir@Co_3O_4 (S) treated group displays the strongest green fluorescence, thus demonstrating the most intense lipid peroxidation of embedded *MRSA* (Figure 5i–k; and Figures S36 and S37, Supporting Information). These data verify that the spiky Ir@Co_3O_4 (S) can effectively penetrate the biofilm, and the induced hole structure facilitates in situ ROS delivery and enhances biofilm eradication.

To further elucidate the mechanism underlying *MRSA* killing and biofilm eradication mediated by Ir@Co_3O_4 (S), comprehensive RNA sequencing (RNA-seq) transcriptomics studies were implemented. We performed a comparative analysis of gene expression profiles in biofilm cells subjected to PBS (control group) or Ir@Co_3O_4 (S). The intersection and disparities in gene expression were visualized through Venn diagrams and volcano plots, which reflect differentially expressed genes (DEGs) between the juxtaposed groups. The analysis unveils 34 DEGs that are upregulated and 215 DEGs that are downregulated within the Ir@Co_3O_4 (S) group compared to the control group (**Figure** 6a,b). The heatmap presents the metabolite disparities across the two groups (Figure 6c).

According to Gene Ontology (GO) analysis, these DEGs correlate with diverse biological processes, cellular components, and molecular functions (Figure 6d). By integrating with GO-enriched bubble plot analysis, we can evidence that biosynthetic processes are considerably affected under Ir@Co_3O_4 (S) treatment, with involvement of cellular amino acid biosynthesis (e.g., hisA and hisH), carboxylic acid biosynthesis (e.g., arcC and hutU), and hemoglobin binding (e.g., isdC). Biosynthesis-related genes are implicated in *MRSA* virulence factors, lipid peroxidation, bacterial nutrient uptake, and metabolism. The inhibition of these genes would substantially impair the capacity of *MRSA* to colonize and reproduce (Figure 6e).[65] Furthermore, we hypothesize that Ir@Co_3O_4 (S) inhibits *MRSA* biofilm activity by intervening in the maintenance of the cellular environment and obstructing bacterial adherence to EPS, such as conservation of intracellular sites (e.g., ftnA), extracellular regions (e.g., sceD), and saccharide synthesis (e.g., isdC). This suppression reduces bacterial virulence and affects biofilm survival by disrupting the agglomerate binding of EPS, thus affecting the survival of the bacterial biofilm.[66]

In addition, the extracted differential metabolites are subsequently analyzed against the Kyoto Encyclopedia of Genes and Genomes (KEGG) and highlight the top 14 metabolic pathways that are downregulated following Ir@Co_3O_4 (S) treatment (Figure 6f). DEGs in the Ir@Co_3O_4 (S) treated group are concentrated in pathways related to amino acid syntheses and metabolisms, such as histidine metabolism and arginine biosynthesis, associated with biofilm formation detachment.[16,67] Furthermore, the inhibition of ABC transporter protein genes (e.g., hisG and ahpF), which control the simultaneous process of ATP hydrolysis and transport, suggests an impact on the *MRSA* nutrient uptake mechanism.[68] To summarize, we conjecture that Ir@Co_3O_4 (S) particles can foster the dispersion and eradication of biofilms by down-regulating the associated genes for the biosynthesis and preservation of both intra- and extracellular environments (Figure 6g).

Before animal experiments, we assessed the biosafety of Ir@Co_3O_4 (S) using human umbilical vein endothelial cells (HUEVCs). As analyzed by the Calcein-AM Live/Dead and Cell Counting Kit-8 (CCK-8) assay kits, all experimental groups display limited short-term toxicity, whereas the cellular activity of HUEVCs recovers significantly after 3 days of incubation and maintains a satisfactory viability (Figures S38 and S39, Supporting Information). Additionally, no hemolysis has been observed for Ir@Co_3O_4 (S), even at a high concentration of 2.4 mg mL^{-1} (Figure S40, Supporting Information), indicating excellent blood compatibility. These results demonstrate that Ir@Co_3O_4 (S) exhibits favorable biocompatibility and biomedical application potential. Considering the superior biosecurity

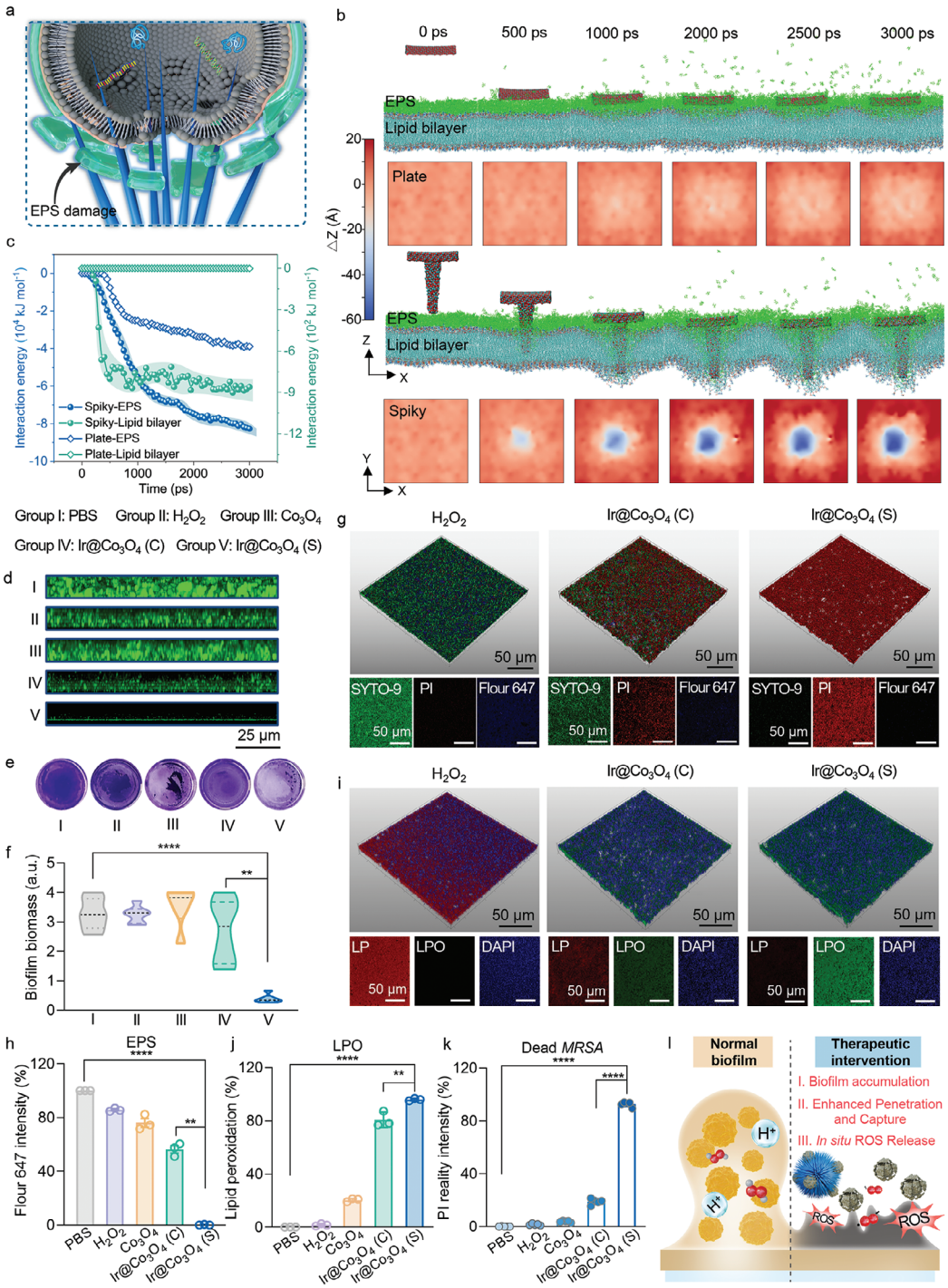

Figure 5. Theoretical and experimental studies on the biofilm penetration and eradication. a) Schematic diagram of EPS and lipid bilayer destruction by puncture of spiky Ir@Co_3O_4 (S). b) Representative snapshots and z-axis top view snapshots of plate and spiky-like materials on EPS and lipid bilayers; data are simulated by molecular dynamics (MD). c) Interaction force profiles with EPS and lipid bilayers during the action of flat and spiky materials. d) z-stack images corresponding to Live/Dead staining of bacteria (scale bar: 25 μm). e) Photographs of biofilms stained by crystal violet. f) Bacterial biomass of biofilms treated with different samples quantified by crystal violet-stained biofilms ($n = 3$ biologically independent replicates). g) Alexa Flour 647 stained confocal microscopy images of different materials cointeracting with *MRSA* biofilms (scale bar: 50 μm). h) Statistics of Alexa Fluor 647 relative intensity ($n = 3$ biologically independent replicates). i) C11-BODIPY$^{581/591}$ stained confocal microscopy images of different materials cointeracting with *MRSA* biofilms (scale bar: 50 μm). j) Calculated statistics on the degree of LPO ($n = 3$ biologically independent replicates). k) PI relative intensity statistics ($n = 3$ biologically independent replicates). l) Schematic diagram for before and after application of Ir@Co_3O_4 (S) biocatalyst to eradicate biofilm. Experiments were repeated independently b, d, e, g, i) three times with similar results. Data are expressed as mean ± S.D. The assessment of *P*-values is performed through the utilization of one-way ANOVA. Indication of significant differences is marked by asterisks (*$P < 0.05$, **$P < 0.01$, ***$P < 0.001$, ****$P < 0.0001$, ns represented nonsignificance). a.u. indicates the arbitrary units.

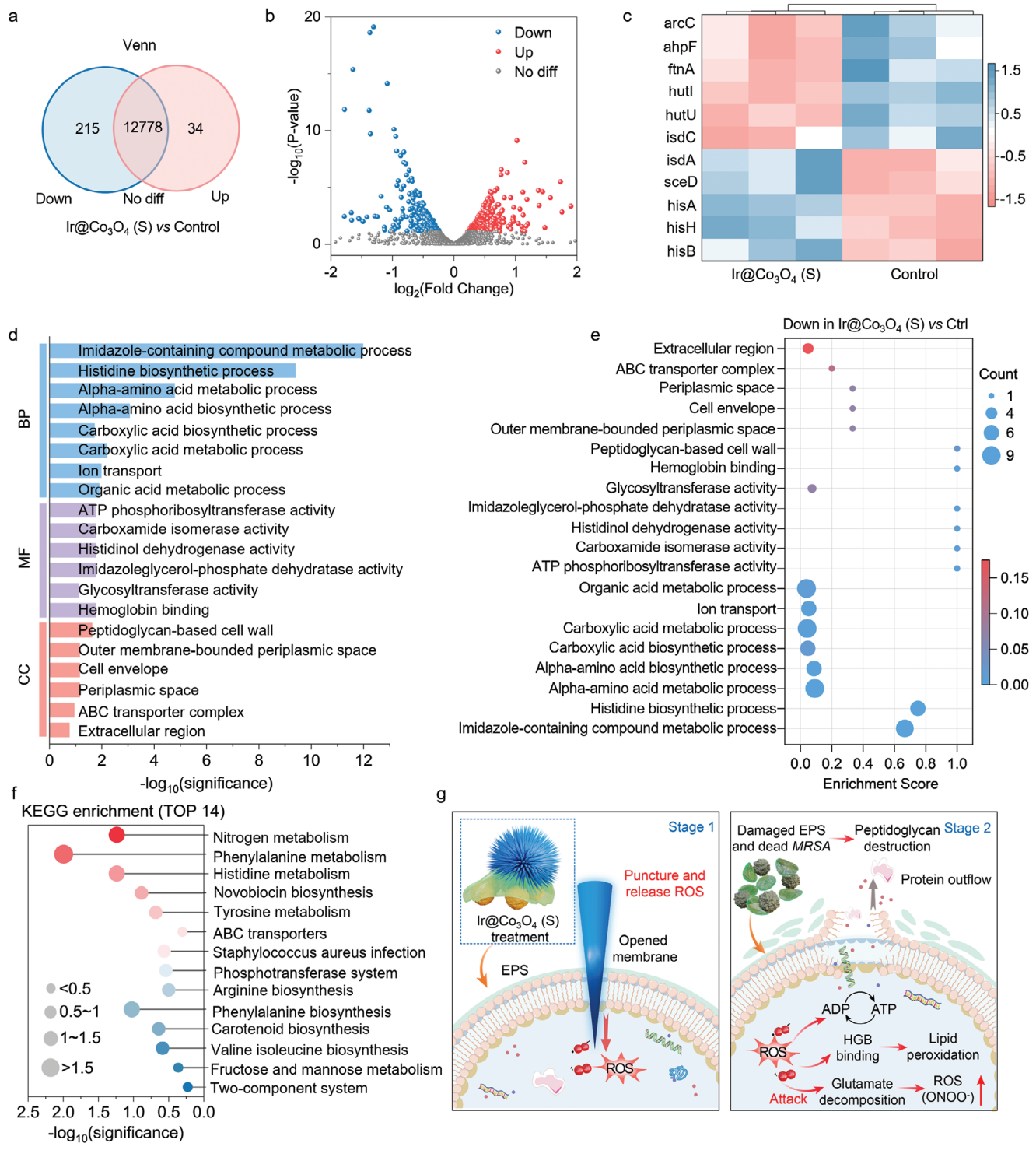

Figure 6. Transcriptomic analysis of *MRSA* killing and biofilm eradication. a) Venn diagram of differentially expressed genes in the $Ir@Co_3O_4$ (S) and PBS (Control) treated groups. b) Volcano plots of differentially expressed genes (gray: not significantly different genes; red: upregulated genes; blue: downregulated genes). c) Heat map of differentially expressed genes involved in bacterial metabolism pathway (red represents genes with relatively high expression levels, blue represents genes with relatively low expression levels). d) GO annotation analysis of DEGs in biofilms treated with $Ir@Co_3O_4$ (S). e) GO enrichment of downregulated genes. f) KEGG enrichment (TOP 14) of downregulated genes. g) Schematic diagram of biofilm penetration and dispersion mechanism by $Ir@Co_3O_4$ (S) particles.

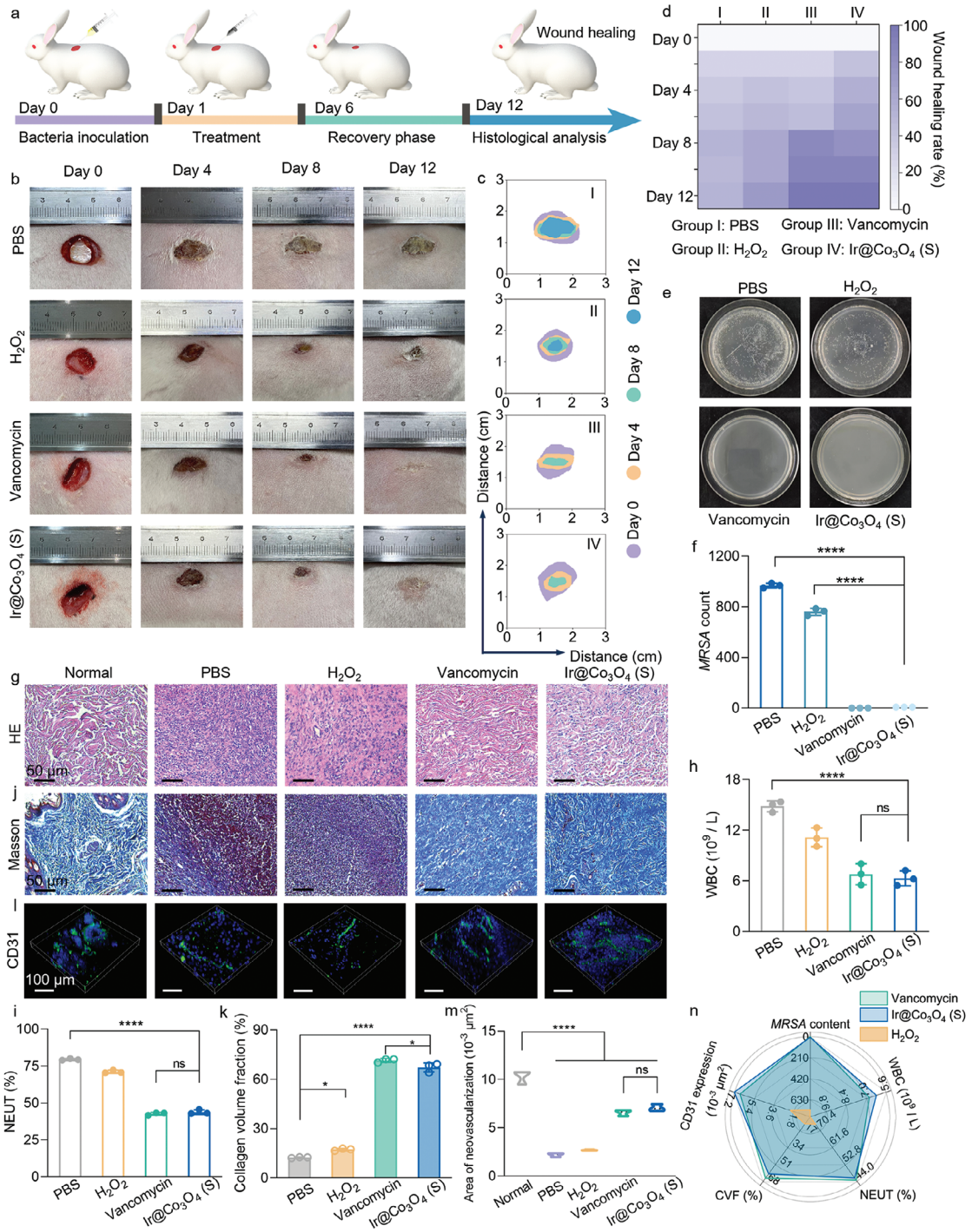

Figure 7. In vivo antibacterial and biofilm eradication effects of artificial phages. a) Schematic illustration of the treatment schedule for the *MRSA*-infected wounds. b) Digital photographs of wound sizes on different days. c) Traces of wound closure over 12 days for groups treated with PBS, H_2O_2, vancomycin, and Ir@Co_3O_4 (S), respectively. d) Wound healing rate after treatment by different systems. e) *MRSA* colonies that were harvested from different groups on day 2. f) The counted bacterial colony numbers in (e) ($n = 3$ biologically independent replicates). g) HE staining images of the epidermal histological sections in different groups after 12 days (scale bar: 50 μm). h) The number of WBCs, and i) the percent of NEUT in peripheral blood ($n = 3$ biologically independent replicates). j) Masson staining images of the epidermal histological sections in different groups after 12 days (scale bar: 50 μm). k) Calculated collagen volume fraction value in j) ($n = 3$ biologically independent replicates). l) CD31 staining images of the epidermal histological sections in different groups after 12 days (scale bar: 100 μm). m) CD31 relative expression in l) ($n = 3$ biologically independent replicates). n) Overall evaluation of the Ir@Co_3O_4 (S), vancomycin, and H_2O_2 for bacterial disinfection. Experiments were repeated independently b, e, g, j, l) three times with similar results. Data are expressed as mean ± S.D. The assessment of *P*-values is performed through the utilization of one-way ANOVA. Indication of significant differences is marked by asterisks (*$P < 0.05$, **$P < 0.01$, ***$P < 0.001$, ****$P < 0.0001$, ns represented nonsignificance). a.u. indicates the arbitrary units.

and desirable antibiofilm activity of Ir@Co_3O_4 (S) against *MRSA* in vitro, we also evaluated the biofilm eradication potency of Ir@Co_3O_4 (S) in vivo employing an *MRSA*-infected rabbit excisional wound model (**Figure** 7a). The infection model was established by inoculating 100 µL of 10^8 CFU mL^{-1} *MRSA* at the wound site, which was subsequently incubated for 24 h to facilitate biofilm formation. The wound was then treated with Ir@Co_3O_4 (S) at a concentration of 0.08 mg mL^{-1}. The photographs and changes in wound sizes were recorded after sterilization treatment (Figure 7b; and Figure S41, Supporting Information). Remarkably, the Ir@Co_3O_4 (S) treated group shows a comparable wound healing rate to the vancomycin-treated group, with full recovery after 12 days. In contrast, both control and H_2O_2-treated groups persistently present wound suppuration, along with abscessed skin and intense inflammation (Figure 7c,d). Subsequently, the volume of *MRSA* on the wounds is quantified through the standard agar plate count technique following wound disinfection treatment, thereby endorsing the in vivo biofilm eradication capacity of Ir@Co_3O_4 (S) (Figure 7e,f).

Moreover, the peripheral tissues from the infectious sites were collected for histopathological analysis on day 12. Hematoxylin and eosin (H&E) staining photographs unveil the presence of numerous nuclei in a lobulated pattern in both PBS and H_2O_2-treated groups, demonstrating an extensive inflammatory cell infiltration.[69] However, the Ir@Co_3O_4 (S) treated group displays successfully controlled inflammation, similar to the vancomycin-treated group (Figure 7g). A comparative hematological analysis of peripheral blood depicts a considerable reduction in white blood cell (WBC) and neutrophils (NEUT) counts for the Ir@Co_3O_4 (S) treated group as compared to the PBS and H_2O_2-treated groups. The WBC and NEUT counts in Figure 7h,i resemble those of the vancomycin-treated group, which correlates with the elimination of residual biofilm infection from the wound without triggering significant inflammation.

Sequentially, Masson trichrome staining analysis of collagen regeneration reveals that the collagen fibers are uniformly and regularly arranged in Ir@Co_3O_4 (S) and vancomycin-treated groups, with dramatically superior deposition than the control and H_2O_2-treated groups (Figure 7j,k). Additionally, the relative CD31 immunofluorescence intensity of Ir@Co_3O_4 (S) (7.06×10^{-3} µm^2) and vancomycin-treated wounds (6.56×10^{-3} µm^2) are markedly increased, reflecting the newly formed blood vessels after wound revascularization, that results in excellent wound recovery (Figure 7l,m; and Figure S42, Supporting Information). Meanwhile, no damage or abnormality was detected in major organs with respect to the healthy group, suggesting that Ir@Co_3O_4 (S) is a relatively secure skin sterilization therapy (Figure S43, Supporting Information). Furthermore, a comparison of the effectiveness of Ir@Co_3O_4 (S), vancomycin, and H_2O_2 in bacterial biofilm eradication and wound healing promotion indicates a similar efficacy of Ir@Co_3O_4 (S) and vancomycin across most therapeutic indexes (Figure 7n). Conclusively, these in vivo sterilization results corroborate the synthesized artificial phage as a potent antibiotic-free agent that is capable of efficiently eradicating *MRSA* biofilm and expediting wound healing with therapeutic effectiveness equivalent to vancomycin.

3. Conclusion

In summary, we have designed and constructed a spiky Ir@Co_3O_4 (S) particle system to serve as an artificial phage for synergistically eradicating antibiotic-resistant *MRSA* biofilms. Benefiting from the synergistic effects of abundant nanospikes and highly active Ir catalytic sites, the synthesized metal oxide-based artificial phage can simultaneously achieve efficient biofilm accumulation, EPS penetration, and superior BME-adaptive ROS generation. Systematic in vitro studies demonstrate that artificial phage can induce hole structure to facilitate in situ ROS delivery and enhance biofilm eradication. Moreover, metabolomics studies evidenced that the accumulation of artificial phage obstructs the bacterial attachment to EPS, disrupts the maintenance of the cellular environment, and promotes the dispersion and eradication of biofilms by down-regulating the associated genes for the biosynthesis and preservation of both intra- and extracellular environments. Our in vivo investigations demonstrate that the artificial phage can eradicate *MRSA* biofilm and expedite wound healing with therapeutic effectiveness equivalent to vancomycin. We anticipate that the design of this spiky artificial phage with synergistic "penetrate and eradicate" capability and pronounced ROS-catalytic activity will not only provide a potential pathway to treat antibiotic-resistant biofilms-induced recalcitrant infected wounds but also open up new avenues for bionic and nonantibiotic disinfection strategies.

4. Experimental Section

Experimental details, including materials, characterizations, synthesis of Co_3O_4, Ir@Co_3O_4 (C), and Ir@Co_3O_4 (S), ROS catalytic assays, and in vitro and in vivo antibacteria experiments, were listed in the Supporting Information.

Animals: Healthy adult New Zealand white rabbits (2.5–3.0 kg, male) were procured from Chengdu Dossy Biological Technology Co. Ltd. (China). All the animal experiments were performed following the animal ethical standards from the Animal Ethics Committee at West China Hospital, Sichuan University, Chengdu, China: the assigned approval number was 20220506003.

Statistical Analysis: All data were expressed in this manuscript as mean ± S.D. All the results were performed at least three times using independent experiments. No samples were excluded from the analysis. The one-way ANOVA analysis was employed for comparison between groups. In all cases, significance was defined as $P \leq 0.05$. Asterisks indicate significant differences (*$P < 0.05$, **$P < 0.01$, ***$P < 0.001$, ****$P < 0.0001$, ns represented nonsignificance). The statistical analysis was carried out using GraphPad Prism 8.0 (GraphPad Software Inc.).

Supporting Information

Supporting Information is available from the Wiley Online Library or from the author.

Acknowledgements

This work was financially supported by the National Key R&D Program of China (No. 2021YFB3800705), National Natural Science Foundations of China (Nos. 82272003, 52173133, 52373148, and 52161145402), Sichuan Science and Technology Program (Nos. 2023YFH0031 and 2023YFH0008), the 1·3·5 Project for Disciplines of Excellence, West China

Hospital, Sichuan University (No. ZYJC21047), the State Key Laboratory of Polymer Materials Engineering (No. sklpme2021-4-02), Fundamental Research Funds for the Central Universities. R.D.R. acknowledges support from the Russian Science Foundation c22-12-20027 and the Tomsk region administration. The authors also gratefully acknowledged Dr. Mi Zhou and Dr. Chao He for their analytical support, and they also thank Li Li, Fei Chen, and Chunjuan Bao of the Institute of Clinical Pathology, Sichuan University, for processing histological staining.

Conflict of Interest

The authors declare no conflict of interest.

Author Contributions

S.T.X. and L.X. contributed equally to this work. S.T.X., L.X., L.Q., and C.C. conceived the idea and designed the project. S.T.X. and L.X. performed the experiments and analyzed the results. W.G. and S.T.X. designed and conducted the DFT theoretical calculations. M.W. and L.X. performed and analyzed MD simulations. Y.G., X.Z.W., R.D.R., and L.C. assisted with the figure production and experimental design. S.T.X., L.X., L.Q., and C.C. wrote the manuscript. L.Q. and C.C. corrected the manuscript and supervised the whole project. All authors discussed the results and commented on the manuscript.

Data Availability Statement

The data that support the findings of this study are available from the corresponding author upon reasonable request.

Keywords

antibacterial and biofilm eradication, artificial phages, biocatalytic materials, reactive oxygen species, wound healing

Received: March 26, 2024
Revised: June 1, 2024
Published online:

[1] O. O. Ikhimiukor, E. E. Odih, P. Donado-Godoy, I. N. Okeke, *Nat. Microbiol.* **2022**, *7*, 757.
[2] H. Wu, M. Wei, S. Hu, P. Cheng, S. Shi, F. Xia, L. Xu, L. Yin, G. Liang, F. Li, D. Ling, *Adv. Sci.* **2023**, *10*, 2301694.
[3] E. D. Brown, G. D. Wright, *Nature.* **2016**, *529*, 336.
[4] Y. Ding, J. Chen, Q. Wu, B. Fang, W. Ji, X. Li, C. Yu, X. Wang, X. Cheng, H.-D. Yu, Z. Hu, K. Uvdal, P. Li, L. Li, W. Huang, *SmartMat.* **2023**, e1214, https://doi.org/10.1002/smm2.1214.
[5] A. Vishwakarma, F. Dang, A. Ferrell, H. A. Barton, A. Joy, *J. Am. Chem. Soc.* **2021**, *143*, 9440.
[6] H. Koo, R. N. Allan, R. P. Howlin, P. Stoodley, L. Hall-Stoodley, *Nat. Rev. Microbiol.* **2017**, *15*, 740.
[7] J. Cheng, G. Gan, S. Zheng, G. Zhang, C. Zhu, S. Liu, J. Hu, *Nat. Commun.* **2023**, *14*, 7510.
[8] D. S. Karaman, U. K. Ercan, E. Bakay, N. Topaloglu, J. M. Rosenholm, *Adv. Funct. Mater.* **2020**, *30*, 1908783.
[9] L. Karygianni, Z. Ren, H. Koo, T. Thurnheer, *Trends Microbiol.* **2020**, *28*, 668.
[10] S. Ghosh, M. Sinha, R. Samanta, S. Sadhasivam, A. Bhattacharyya, A. Nandy, S. Saini, N. Tandon, H. Singh, S. Gupta, A. Chauhan, K. K. Aavula, S. S. Varghese, P. Shi, S. Ghosh, M. K. Garg, T. Saha, A. Padhye, S. Ghosh, H. L. Jang, S. Sengupta, *Nat. Biomed. Eng.* **2022**, *6*, 1180.
[11] K. Sauer, P. Stoodley, D. M. Goeres, L. Hall-Stoodley, M. Burmolle, P. S. Stewart, T. Bjarnsholt, *Nat. Rev. Microbiol.* **2022**, *20*, 608.
[12] L. Tan, J. Fu, F. Feng, X. Liu, Z. Cui, B. Li, Y. Han, Y. Zheng, K. W. K. Yeung, Z. Li, S. Zhu, Y. Liang, X. Feng, X. Wang, S. Wu, *Sci. Adv.* **2020**, *6*, eaba5723.
[13] K. P. Rumbaugh, K. Sauer, *Nat. Rev. Microbiol.* **2020**, *18*, 571.
[14] W. Liu, R. Gao, C. Yang, Z. Feng, W. Ou-Yang, X. Pan, P. Huang, C. Zhang, D. Kong, W. Wang, *Sci. Adv.* **2022**, *8*, eabn7006.
[15] H. Hu, D. Li, W. Dai, Q. Jin, D. Wang, J. Ji, B. Z. Tang, Z. Tang, *Adv. Funct. Mater.* **2023**, *33*, 2213134.
[16] Z. Liu, K. Guo, L. Yan, K. Zhang, Y. Wang, X. Ding, N. Zhao, F.-J. Xu, *Nat. Commun.* **2023**, *14*, 5132.
[17] C. Yang, Y. Luo, H. Shen, M. Ge, J. Tang, Q. Wang, H. Lin, J. Shi, X. Zhang, *Nat. Commun.* **2022**, *13*, 4866.
[18] L. Wang, F. Gao, A. Wang, X. Chen, H. Li, X. Zhang, H. Zheng, R. Ji, B. Li, X. Yu, J. Liu, Z. Gu, F. Chen, C. Chen, *Adv. Mater.* **2020**, *32*, 2005423.
[19] H. Huang, W. Geng, X. Wu, Y. Zhang, L. Xie, T. Ma, C. Cheng, *Angew. Chem., Int. Ed.* **2023**, *63*, 202310811.
[20] S. J. Cao, Y. P. Long, S. T. Xiao, Y. T. Deng, L. Ma, M. Adeli, L. Qiu, C. Cheng, C. S. Zhao, *Chem. Soc. Rev.* **2023**, *52*, 6838.
[21] H. C. Parkin, S. T. G. Street, B. Gowen, L. H. Da-Silva-Correa, R. Hof, H. L. Buckley, I. Manners, *J. Am. Chem. Soc.* **2024**, *146*, 5128.
[22] B. Yu, W. Wang, W. Sun, C. Jiang, L. Lu, *J. Am. Chem. Soc.* **2021**, *143*, 8855.
[23] R. Wang, M. Shi, F. Xu, Y. Qiu, P. Zhang, K. Shen, Q. Zhao, J. Yu, Y. Zhang, *Nat. Commun.* **2020**, *11*, 4465.
[24] H. Zhu, B. Li, X. Liu, Y. Qiao, Y. Lv, Y. Zheng, Z. Li, Z. Cui, J. Shen, S. Wu, *ACS Nano.* **2022**, *16*, 21098.
[25] J. Li, S. Song, J. Meng, L. Tan, X. Liu, Y. Zheng, Z. Li, K. W. K. Yeung, Z. Cui, Y. Liang, S. Zhu, X. Zhang, S. Wu, *J. Am. Chem. Soc.* **2021**, *143*, 15427.
[26] J. M. V. Makabenta, A. Nabawy, C. H. Li, S. Schmidt-Malan, R. Patel, V. M. Rotello, *Nat. Rev. Microbiol.* **2021**, *19*, 23.
[27] Y. Wu, P. Liu, B. Mehrjou, P. K. Chu, *Adv. Mater.* **2024**, *36*, 2305940.
[28] M. Yuan, Q. Li, Y. Gao, C. He, M. Adli, C. Wu, H. Zhou, X. Luo, L. Ma, C. Cheng, *Adv. Funct. Mater.* **2023**, *33*, 2304271.
[29] F. Gao, T. Shao, Y. Yu, Y. Xiong, L. Yang, *Nat. Commun.* **2021**, *12*, 745.
[30] Y. Guo, S. Ding, C. Shang, C. Zhang, M. Li, Q. Zhang, L. Gu, B. C. Heng, S. Zhang, F. Mei, Y. Huang, X. Zhang, M. Xu, J. Jiang, S. Guo, X. Deng, L. Chen, *Adv. Mater.* **2023**, *36*, 2306292.
[31] B. A. Pettygrove, R. M. Kratofil, M. Alhede, P. o. Jensen, M. Newton, K. Qvortrup, K. B. Pallister, T. Bjarnsholt, P. Kubes, J. M. Voyich, P. S. Stewart, *Biomaterials.* **2021**, *275*, 120775.
[32] Y. Huang, Y. Liu, N. Pandey, S. Shah, A. Simon-Soro, J. Hsu, Z. Ren, Z. Xiang, D. Kim, T. Ito, M. J. Oh, C. Buckley, F. Alawi, Y. Li, P. Smeets, S. Boyer, X. Zhao, D. Joester, D. Zero, D. Cormode, H. Koo, *Nat. Commun.* **2023**, *14*, 6087.
[33] L. Zhang, H. Wang, X. Qu, *Adv. Mater.* **2023**, *36*, 2211147.
[34] J.-X. An, Z.-Y. Han, Y.-T. Qin, C.-X. Li, J.-L. He, X.-Z. Zhang, *Adv. Mater.* **2023**, *36*, 2305384.
[35] L. S. Babonis, C. Enjolras, A. J. Reft, B. M. Foster, F. Hugosson, J. F. Ryan, M. Daly, M. Q. Martindale, *Nat. Commun.* **2023**, *14*, 885.
[36] F. Zurabov, E. Glazunov, T. Kochetova, V. Uskevich, V. Popova, *Sci. Rep.* **2023**, *13*, 15188.
[37] E. Maffei, A.-K. Woischnig, M. R. Burkolter, Y. Heyer, D. Humolli, N. Thurkauf, T. Bock, A. Schmidt, P. Manfredi, A. Egli, N. Khanna, U. Jenal, A. Harms, *Nat. Commun.* **2024**, *15*, 175.
[38] C. Gong, W. Guan, X. Liu, Y. Zheng, Z. Li, Y. Zhang, S. Zhu, H. Jiang, Z. Cui, S. Wu, *Adv. Mater.* **2022**, *34*, 2206134.
[39] Y. Xie, S. Xiao, L. Huang, J. Guo, M. Bai, Y. Gao, H. Zhou, L. Qiu, C. Cheng, X. Han, *ACS Nano.* **2023**, *17*, 15097.
[40] Y. Lu, T. Liu, C. L. Dong, Y. C. Huang, Y. Li, J. Chen, Y. Zou, S. Wang, *Adv. Mater.* **2021**, *33*, 2007056.

[41] Y. Zhu, J. Wang, T. Koketsu, M. Kroschel, J.-M. Chen, S.-Y. Hsu, G. Henkelman, Z. Hu, P. Strasser, J. Ma, *Nat. Commun.* **2022**, *13*, 7754.
[42] H. Li, C. Chen, Y. Yan, T. Yan, C. Cheng, D. Sun, L. Zhang, *Adv. Mater.* **2021**, *33*, 2105067.
[43] T. Liu, S. Xiao, N. Li, J. Chen, X. Zhou, Y. Qian, C.-H. Huang, Y. Zhang, *Nat. Commun.* **2023**, *14*, 2881.
[44] Y. Zhai, C. Jin, Q. Xia, W. Han, J. Wu, X. Zhao, X. Zhang, *Adv. Funct. Mater.* **2023**, *34*, 2311063.
[45] X.-D. Zhu, Q. Zhang, X. Yang, Y. Wang, J. Wu, J. Gao, J.-J. Zou, G. Wu, Y.-C. Zhang, *SusMat.* **2023**, *3*, 334.
[46] Y. Zhang, S. Zhang, J. Ma, X. Chen, C. Nan, C. Chen, *Angew. Chem., Int. Ed.* **2023**, *135*, 202218926.
[47] X. Wang, Q. Li, Z. Zhao, L. Yu, S. Wang, H. Pu, M. Adeli, L. Qiu, P. Gu, L. Li, C. Cheng, *Adv. Funct. Mater.* **2023**, *34*, 2313143.
[48] X. Wang, X. J. Gao, L. Qin, C. Wang, L. Song, Y.-N. Zhou, G. Zhu, W. Cao, S. Lin, L. Zhou, K. Wang, H. Zhang, Z. Jin, P. Wang, X. Gao, H. Wei, *Nat. Commun.* **2019**, *10*, 704.
[49] T. Li, Y. Deng, Z. Xing, S. Xiao, S. Mu, T. Wang, Y. Gao, L. Ma, C. Cheng, C. Zhao, *Small Methods.* **2023**, *7*, 2300011.
[50] L. Li, L. Cao, X. Xiang, X. Wu, L. Ma, F. Chen, S. Cao, C. Cheng, D. Deng, L. Qiu, *Adv. Funct. Mater.* **2022**, *32*, 2107530.
[51] L. Li, S. Cao, Z. Wu, R. Guo, L. Xie, L. Wang, Y. Tang, Q. Li, X. Luo, L. Ma, C. Cheng, L. Qiu, *Adv. Mater.* **2022**, *34*, 2108646.
[52] H. Zhu, J. Deng, M. Yuan, X. Rong, X. Xiang, F. Du, X. Luo, C. Cheng, L. Qiu, *Small.* **2023**, *19*, 2206911.
[53] J. Zielonka, J. Vasquez-Vivar, B. Kalyanaraman, *Nat. Protoc.* **2008**, *3*, 8.
[54] X. Lu, L. Kuai, F. Huang, J. Jiang, J. Song, Y. Liu, S. Chen, L. Mao, W. Peng, Y. Luo, Y. Li, H. Dong, B. Li, J. Shi, *Nat. Commun.* **2023**, *14*, 6767.
[55] J. Shin, D. W. Kang, J. H. Lim, J. M. An, Y. Kim, J. H. Kim, M. S. Ji, S. Park, D. Kim, J. Y. Lee, J. S. Kim, C. S. Hong, *Nat. Commun.* **2023**, *14*, 1498.
[56] Y. Deng, Y. Gao, T. Li, S. Xiao, M. Adeli, R. D. Rodriguez, W. Geng, Q. Chen, C. Cheng, C. Zhao, *ACS Nano.* **2023**, *17*, 2943.
[57] Y. Q. Qiao, X. M. Liu, B. Li, Y. Han, Y. F. Zheng, K. W. K. Yeung, C. Y. Li, Z. D. Cui, Y. Q. Liang, Z. Y. Li, S. L. Zhu, X. B. Wang, S. L. Wu, *Nat. Commun.* **2020**, *11*, 4446.
[58] X. Fan, F. Yang, J. B. Huang, Y. Yang, C. X. Nie, W. F. Zhao, L. Ma, C. Cheng, C. S. Zhao, R. Haag, *Nano Lett.* **2019**, *19*, 5885.
[59] Y. Huang, Q. Gao, C. Li, X. Chen, X. Li, Y. He, Q. Jin, J. Ji, *Adv. Funct. Mater.* **2022**, *32*, 2109011.
[60] M. Zhang, J. Cheng, Z. Shen, P. Lin, S. Ding, J. Hu, *Angew. Chem., Int. Ed.* **2023**, *62*, 202314563.
[61] Y. Chen, Z. Yang, S. Wang, Q. Ma, L. Li, X. Wu, Q. Guo, L. Tao, X. Shen, *Adv. Healthcare Mater.* **2023**, *12*, 2202150.
[62] D. Hu, L. Zou, W. Yu, F. Jia, H. Han, K. Yao, Q. Jin, J. Ji, *Adv. Sci.* **2020**, *7*, 2000398.
[63] J. Y. Jo, A. Price-Whelan, L. E. P. Dietrich, *Nat. Rev. Microbiol.* **2022**, *20*, 593.
[64] W. Kulig, M. Pasenkiewicz-Gierula, T. Rog, *Data Brief.* **2015**, *5*, 333.
[65] N. Butler, A. M. Kunjapur, *J. Biotechnol.* **2020**, *307*, 1, http://doi.org/10.1016/j.jbiotec.2019.10.002.
[66] H. T. Chen, C. Q. Yu, H. Wu, G. Q. Li, C. R. Li, W. Hong, X. Y. Yang, H. Wang, X. F. You, *Front. Chem.* **2022**, *10*, 866392.
[67] J. W. Sun, S. T. Rutherford, T. J. Silhavy, K. C. Huang, *Nat. Rev. Microbiol.* **2022**, *20*, 236.
[68] D. C. Rees, E. Johnson, O. Lewinson, *Nat. Rev. Mol. Cell Biol.* **2009**, *10*, 218.
[69] X. Y. Bao, S. Q. Zheng, L. Zhang, A. Z. Shen, G. Y. Zhang, S. Y. Liu, J. M. Hu, *Angew. Chem., Int. Ed.* **2022**, *61*, 202207250.